



UNIVERSITY OF LEEDS

This is a repository copy of *Composition and structure of an 18-year-old 5M KOH-activated ground granulated blast-furnace slag paste*.

White Rose Research Online URL for this paper:
<http://eprints.whiterose.ac.uk/128168/>

Version: Accepted Version

Article:

Richardson, IG and Li, S (2018) Composition and structure of an 18-year-old 5M KOH-activated ground granulated blast-furnace slag paste. *Construction and Building Materials*, 168. pp. 404-411. ISSN 0950-0618

<https://doi.org/10.1016/j.conbuildmat.2018.02.034>

© 2018. This manuscript version is made available under the CC-BY-NC-ND 4.0 license
<http://creativecommons.org/licenses/by-nc-nd/4.0/>

Reuse

This article is distributed under the terms of the Creative Commons Attribution-NonCommercial-NoDerivs (CC BY-NC-ND) licence. This licence only allows you to download this work and share it with others as long as you credit the authors, but you can't change the article in any way or use it commercially. More information and the full terms of the licence here: <https://creativecommons.org/licenses/>

Takedown

If you consider content in White Rose Research Online to be in breach of UK law, please notify us by emailing eprints@whiterose.ac.uk including the URL of the record and the reason for the withdrawal request.



eprints@whiterose.ac.uk
<https://eprints.whiterose.ac.uk/>

1 **Title:** Composition and structure of an 18-year-old 5M KOH-activated ground
2 granulated blast-furnace slag paste.

3

4 **Authors:** I.G. Richardson, S. Li¹

5

6 **Address:** School of Civil Engineering, University of Leeds, Leeds, West Yorkshire, LS2
7 9JT, United Kingdom.

8

9 **Email:** i.g.richardson@leeds.ac.uk

10

11 **Abstract**

12 The main hydration products were C-A-S-H(I), present in both inner (Ip) and outer
13 product (Op), and a Mg-Al layered double hydroxide (LDH), present only in the Ip. The
14 composition of C-A-S-H(I) was the same in Op and Ip. Reduced scatter in the data with
15 age suggests a tendency towards compositional homogeneity. The mean length of the
16 aluminosilicate anions in the C-A-S-H(I) increased with age. The layer spacings of the C-
17 A-S-H(I) and Mg-Al LDH had not changed significantly with age. The Mg/Al ratio of the
18 LDH was about 2.6 and had not changed between 1 and 18 years.

19 **Keywords:** slag, NMR, TEM, microstructure, alkali activation

¹ Present address: School of Civil Engineering, Haerbin Institute of Technology, Haerbin, Heilongjiang, 150000, China.

20 **1. Introduction**

21 UK Government policy is for the disposal of higher activity waste through geological
22 disposal [1]. Cementitious materials play a key role in the engineered components of a
23 geological disposal facility (GDF), in particular as waste encapsulation grouts, buffers
24 and backfills, fracture grouts, waste containers and overpacks, tunnel plugs, and
25 tunnel/vault linings, etc. [2-5]. Cementitious materials have many advantages for use in
26 the disposal of radioactive wastes: for example, by providing containment of
27 radionuclides in the long term by ensuring low solubility for most radionuclides because
28 of the alkaline chemistry of the cement and in assisting immobilisation of radionuclides
29 through structural accommodation in hydration products [6]. A range of cementitious
30 materials are considered for use in the GDF, including ordinary Portland cement (oPc),
31 oPc blended with ground granulated blast-furnace slag (ggbs) and oPc blended with
32 pulverized fuel ash (pfa) [7]. In this context, studies concerned with the activation of
33 ggbs were initiated in the UK in the early 1980s with the aim of identifying the hydration
34 products and providing insight into the mechanism of hydration. As part of this work,
35 Wilding and McHugh [8] reported results of early-age studies of the hydration of a
36 number of blast-furnace slag cements hydrated for up to 1 year; systems included oPc-
37 ggbs blends with 0, 50, 67, 75, and 90% slag, and ggbs activated with $\text{Ca}(\text{OH})_2$ or KOH
38 solution. The last of these involved solution concentrations of 1M, 2.5M, 3.75M, 5M and
39 10M. Wilding & McHugh employed isothermal conduction calorimetry, differential
40 scanning calorimetry and powder X-ray diffraction. Richardson and co-workers
41 extended the work of Wilding & McHugh – using the same ggbs – to greater ages, up to
42 3.5 years for the blended cements [9-11] and 8 years for a 5M KOH-activated ggbs paste
43 [12], which involved the most comprehensive application to date of analytical
44 transmission electron microscopy to the study of hardened oPc and oPc-ggbs cement

45 pastes [10-12]. The work on blended cements has since been extended to 20 years [13,
46 14] and the purpose of the present paper is to report the results of the examination of
47 the 5M KOH-activated ggbs paste after ageing for a further 10 years (i.e. after 18 years).
48 Extensive work is being conducted worldwide on alkali-activated cements, largely as a
49 consequence of efforts to address the significant level of anthropogenic carbon dioxide
50 that is associated with the manufacture of Portland cement [15], and the results of the
51 present study are relevant to that work, which has been the subject of numerous
52 reviews, e.g. [16].

53 **2. Material and methods**

54 **2.1 Preparation of specimens**

55 The oxide composition that was supplied with the anhydrous ggbs is given in [10] (a
56 “Cemsave” ggbs supplied by the Frodingham Cement Co. Ltd., Scunthorpe, UK). XRD
57 showed that the ggbs was largely glassy with a small amount of melilite [8] (the pattern
58 extracted from [8] is inset on Fig. 1, labelled “S”). The composition of the glassy slag was
59 determined by electron microprobe analysis of powder, embedded in resin, ground and
60 polished flat; the details are given in [14] and in summary: Ca/Si = 1.09 ± 0.06 ;
61 Ca/(Al+Si) = 0.80 ± 0.04 ; Al/Si = 0.37 ± 0.02 ; Mg/Si = 0.32 ± 0.02 (mean atom ratios ± 1
62 standard deviation; $n = 392$ particles). The ggbs had a typical cumulative particle size
63 distribution, which is shown in Fig. 2 (determined by laser granulometry). The ggbs
64 powder was mixed with 5M KOH solution at a solution/solid ratio of 0.4 (mL g⁻¹) for five
65 minutes. The resulting slurry was placed in polythene tubes, which were then sealed in a
66 plastic bag before placing in a curing bath, set at 20°C, where they remained for 5 years
67 5 months, after which the packs were removed from the water bath and stored – kept

68 sealed in the tubes and the plastic bags – in the ambient environment conditions of an
69 office at the University of Leeds.

70

71 **2.2 Experimental techniques**

72 The sample was characterized using a number of techniques: simultaneous thermal
73 analysis (STA), powder X-ray diffraction (XRD), analytical scanning and transmission
74 electron microscopy (SEM and TEM), and solid-state single-pulse ^{29}Si and ^{27}Al magic
75 angle spinning (MAS) nuclear magnetic resonance spectroscopy (NMR).

76 The STA (Stanton Redcroft STA1500) was equipped with simultaneous thermo-
77 gravimetric (TG) and differential thermal analysis (DTA). The sample was freshly
78 crushed and ground to a powder in an agate mortar; it was heated to 1000 °C at
79 20 °C/min, under a constant flow of N_2 gas. An evolved gas analysis (EGA) system
80 (Cirrus mass spectrometer, MKS Spectra Products Ltd., U.K.) interfaced with the STA
81 equipment was used to differentiate mass loss associated with water or carbon dioxide:
82 in fact, CO_2 was not detected in the sample thus confirming that no carbonation occurred
83 during sample storage or preparation.

84 Powder X-ray diffraction was undertaken using a PANalytical X'Pert Pro theta-theta
85 PW3050/60 diffractometer (480 mm diameter) with PW3064 sample spinner (spun at
86 15 revolutions per minute) and X'Celerator real time multiple strip detector (2.122°
87 active length) in Bragg-Brentano geometry employing a Cu X-ray tube (generator
88 operating at 40 kV and 40 mA) producing K_α radiation ($K_{\alpha 1} = 1.540598 \text{ \AA}$, $K_{\alpha 2} =$
89 1.544426 \AA) and with a Ni K_β absorber (0.02 mm thickness; $K_\beta = 1.39225 \text{ \AA}$). The setup
90 included an incident beam Soller slit of 0.04 rad, incident beam mask of 10 mm and

91 programmable automated divergence slit giving a constant illuminated length of 10 mm,
92 and receiving Soller slit of 0.04 rad. Data acquisition was carried out in continuous scan
93 mode over the range 5.01 to 89.99 °2θ with a step width of 0.01671° (i.e. 5085 steps)
94 and a counting time of 500 s, corresponding to a total acquisition time of 5.7 hours.

95 The sample was demoulded, freshly crushed and ground to fine powder using an agate
96 mortar and pestle.

97 The composition and distribution of phases in the paste were investigated using a
98 Philips XL30 environmental scanning electron microscope (ESEM), operated in
99 backscattered electron mode (BSE) under high vacuum at an acceleration voltage of 20
100 kV. Images were acquired using spot size 5 and at a working distance of 7.5 mm. Details
101 of the method used for specimen preparation are given in [13].

102 TEM-EDX was used to examine the morphology of the hydration products and to
103 determine the chemical composition of the C–A–S–H free of intermixture with other
104 phases (Philips CM20, Eindhoven, Netherlands, equipped with an UTW EDX detector,
105 Oxford, UK, and ISIS software for imaging/X-ray analysis, Oxford Instruments). Details of
106 the method used for specimen preparation are given in [13]. Electron-beam damage was
107 minimized when taking micrographs by using a counting time of less than 20 s real-time
108 and during EDX by analyzing regions that were about 200 nm diameter and using spot
109 size 6.

110 The solid-state MAS NMR spectra were acquired using a Varian InfinityPlus 300
111 spectrometer (magnetic field 7.05 T; operating frequencies of 59.56 MHz for ²⁹Si and
112 78.12 MHz for ²⁷Al). For ²⁹Si, the sample was freshly ground and packed into a 6 mm
113 zirconia rotor sealed at either end with Teflon end plugs, and spun at 7 kHz in a

114 Chemagnetics-style probe. The spectrum was acquired using a pulse recycle delay of 5 s,
115 a pulse width 6 μ s, and an acquisition time of 20.48 ms; 17000 scans were collected,
116 giving a total experiment time of 23.7 hours. The spectrum was fitted to Voigt lineshapes
117 using Igor Pro 5.0 (WaveMetrics, Inc., Lake Oswego, Oregon 97035, USA). For ^{27}Al , the
118 sample was packed into a 3.2 mm rotor and the spectrum was acquired during the first
119 hour of spinning to avoid dehydration of any AFm present in the sample, which can
120 occur with prolonged spinning [19]. The spectrum was thus acquired over 7000 scans
121 using a pulse recycle delay of 0.5 s, a pulse width of 3 μ s and an acquisition time of 10.24
122 ms. Chemical shifts for aluminium are referenced to 1M $[\text{Al}(\text{H}_2\text{O})_6]^{3+}(\text{aq})$ and for silicon
123 are referenced to tetramethyl silane using belite as an external reference ($\delta = -71.3$
124 ppm).

125 **3. Results and discussion**

126 **3.1 Hydration products**

127 Wilding and McHugh [8] showed that the two main hydration products in KOH-activated
128 ggbs pastes are a semi-crystalline C-S-H(I) (it is now known to be more correctly
129 referred to in these systems as C-A-S-H(I) because of the important substitution of Al for
130 Si [20]) and a phase that is related to the mineral hydrotalcite, which is a Mg-Al layered
131 double hydroxide (LDH) phase. The XRD pattern that is shown on Fig. 1 plotted
132 between 5–70° 2 θ shows that this was still the case after 18 years. The STA curves on
133 Fig. 3 are consistent with this conclusion: the large, low-temperature (<300 °C)
134 endotherm is due predominantly to the C-A-S-H(I), with a contribution from the loss of
135 molecular water from the interlayer of the Mg-Al LDH (the high-temperature shoulder),
136 and the endotherm at about 420 °C due to dehydroxylation of the Mg-Al LDH [21].

137 The three inset patterns plotted on Fig. 1 between $4\text{--}14^\circ 2\theta$ are for 5M KOH-activated
138 pastes using the same ggbs hydrated for 7 days (labelled “7d”), 4 months (“4m”), and 8
139 years (“8y”); again, the layer-spacings for the C-A-S-H(I) and Mg-Al LDH phases are
140 indicated for those ages. It is evident that the layer spacing of the main binding phase, C-
141 A-S-H(I), did not change between 4 months and 18 years, at $\approx 12.7 \text{ \AA}$. This value is typical
142 for C-(A-)S-H(I) phases and notably different from the 1.1 nm tobermorites. The
143 situation is similar for the Mg-Al LDH, which had a layer spacing of about 7.7 \AA at all
144 ages; the very slightly lower values measured at intermediate ages are probably due to
145 the effect of overlap from the peak for the layer spacing of an AFm (AFm phases are Ca-
146 Al LDH phases), which occurs as a pronounced low-angle shoulder at those ages. The
147 shoulder on the pattern for the 8-year-old paste indicates a peak at about 7.9 \AA , which
148 would be consistent with the basal reflection for C_4AH_{13} [22]. However, the layer spacing
149 of AFm phases is highly variable, being dependent on the amount of interlayer water and
150 the type of interlayer anions [23], and analyses of AFm plates present in the 8-year-old
151 paste indicated that the AFm probably contained some Si [12]. A reduced quantity of
152 AFm in the oldest paste is consistent with the appearance of small peaks attributable to
153 a hydrogarnet phase [24, 25]; the same thing was observed by Wilding and McHugh [8]
154 when the slag was activated by 7.5M and 10M KOH solution, and hydrogarnet has been
155 observed previously in NaOH-activated pastes, e.g. [26].

156 LDH phases are derived from layered divalent metal hydroxides by the substitution of a
157 fraction (x) of the divalent cations (M^{2+}) by trivalent cations (M^{3+}), which creates a +1
158 charge on the main layer that must be balanced by anions (A^{n-}) in an interlayer region,
159 which also contains water molecules. A^{n-} can be single anions (such as Cl^- or OH^-),
160 trigonal planar anions (CO_3^{2-} , NO_3^-), tetrahedral anions (SO_4^{2-} , CrO_4^{2-}), octahedral
161 anions, or alumino-silicate sheets [27]. The general formula for LDH phases is:

162
$$[M_{(1-x)}^{2+}M_x^{3+}(OH)_2](A^{n-})_{\frac{x}{n}} \cdot mH_2O \quad (1)$$

163 This formula is based on one main-layer cation; the contents of the main layer are within
 164 the square brackets. The number of water molecules per cation, m , is variable.

165 The Mg-Al LDH in slag-containing cements is often referred to as a 'hydrotalcite-like'
 166 phase [23]. However, since the interlayer anion in hydrotalcite is CO_3^{2-} and is likely to be
 167 OH^- in the LDH that is present in alkali-hydroxide activated ggbs pastes (unless affected
 168 by carbonation), any comparison with a natural mineral is more correctly done with
 169 meixnerite ($Mg_6Al_2(OH)_{16}(OH)_2 \cdot 4H_2O$) rather than with hydrotalcite
 170 ($Mg_6Al_2(OH)_{16}(CO_3) \cdot 4H_2O$). This point is supported by the absence of CO_2 on the EGA
 171 plot in Fig. 3.

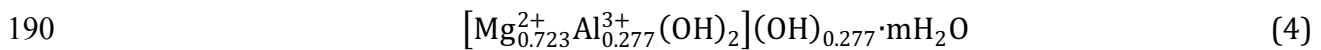
172 Richardson [28] showed that the a parameter of the unit cell of an LDH phase is related
 173 to x by Eq (2), where α is the angle between two oxygen sites and the metal site when
 174 the two oxygen atoms are in the same basal plane (see Fig. 1 of [28]), $r(M^{2+})$ and $r(M^{3+})$
 175 are the effective ionic radii of the cations (values given in [29]), and $r(OH^-)$ is the
 176 effective radius of the oxygen atom of the hydroxyl ion.

177
$$a = 2 \sin\left(\frac{\alpha}{2}\right) \left(r(M^{2+}) + r(OH^-) \right) - 2 \sin\left(\frac{\alpha}{2}\right) \left(r(M^{2+}) - r(M^{3+}) \right) x \quad (2)$$

178 Richardson [28] showed that for LDH phases in general $r(OH^-) = 1.365 \text{ \AA}$ and that $\alpha =$
 179 97.41° for Mg-based LDH phases. Substitution of these values into Eq. (2) together with
 180 Shannon's [29] values for $r(Mg^{2+(VI)})$ and $r(Al^{3+(VI)})$ gives Eq. (3).

181
$$a_{MgLDH} = 3.133 - 0.278x \quad (3)$$

182 Richardson [28] noted that such an equation enables the calculation of the composition
 183 (x) of the LDH from the a parameter, or *vice versa*, whichever is known with most
 184 confidence. In the present case, the powder XRD pattern (shown in Fig. 1) has good
 185 signal-to-noise ratio and calibration of the pattern was achieved using another run for
 186 the same sample, but that included some quartz. The a parameter for the LDH phase is
 187 calculated from d_{110} ($a = 2 \times d_{110}$), which was determined as 1.528 Å (it is indicated on
 188 Fig. 1) and so $a = 3.056$ Å. Substitution of this value into Eq. 3 gives $x = 0.277$ and so the
 189 Mg/Al ratio of the LDH from the XRD pattern is 2.61 and the formula is:



191 In addition to the peaks for the C-A-S-H(I) and Mg-Al LDH phases, the main pattern on
 192 Fig. 1 also has some small but very sharp peaks that correspond to large crystals of
 193 calcite (that display preferred orientation); given the long duration of the experiment it
 194 is conceivable that some carbonation of the sample occurred during data collection, but
 195 such crystals would be expected to be small and so the source of the calcite is uncertain.
 196 It is relevant to note that a preliminary XRD experiment that took only 41 minutes (5-
 197 90 °2 θ) showed no sign of carbonation and the peak positions for the C-A-S-H(I) and the
 198 Mg-Al LDH were the same as with the long duration experiment (obviously the signal-to-
 199 noise ratio was not as good). There is also the possibility of the presence of a minor
 200 amount of a hydrogarnet phase that has a small crystal size (it is possible that the small,
 201 broad peak at about 17.3 °2 θ – that is superposed on a larger C-A-S-H(I) peak – is the
 202 112 peak of a hydrogarnet phase) and there is a trace of quartz, perhaps due to slight
 203 contamination picked up during sample grinding (the agate mortar that is used for
 204 grinding is cleaned using sand, although it should of course have been subsequently
 205 washed). The broad hump on the pattern between about 20° and 40° 2 θ is perhaps due

206 in part to some C-A-S-H that is not as well ordered as the C-A-S-H(I), but there will
207 certainly be a significant contribution from unreacted ggbs (see the “S” inset on Fig. 1;
208 deconvolution of the ^{29}Si NMR spectrum indicates that about one fifth of the slag
209 remains unreacted; see §3.4).

210 **3.2 Microstructure**

211 The microstructural features in slag-KOH pastes can be classified in the same way as in
212 other hydrated cements using Taplin’s inner product (Ip)/outer product (Op) schema
213 [30], where inner products form within the volume of the original particles and outer
214 products form in the volume originally occupied by solution. This is illustrated in Fig. 4,
215 which is a typical backscattered electron image from the sample that shows a partially
216 reacted slag grain (unreacted slag labelled “S”, surrounding Ip labelled “Ip1”), fully
217 reacted slag (e.g. region labelled “Ip2”), and outer product (e.g. region labelled “Op”).
218 The Ip regions appear slightly darker than the Op regions, which is probably caused by
219 differences in chemical composition rather than density; this is discussed further in §3.3.
220 The angular shape of the original slag particles is evident for both fully and partially
221 reacted particles. The features present in Fig. 4 are similar to those on a micrograph for
222 a 1-month-old KOH-activated ggbs mortar [31].

223

224 Fig. 5 is a typical TEM micrograph that shows foil-like Op C-A-S-H(I) between two
225 regions of Ip that has a generally fine, homogeneous morphology but with some lath-like
226 features that are associated with the Mg-Al LDH phase; any pores within this Ip are very
227 small. The foil-like morphology of the Op C-A-S-H(I) is not only distinctly different from
228 the fibrillar morphology that is typical of Op C-S-H produced by Portland cement

229 hydration [11], but it is also less crumpled than the Op C-A-S-H foils that are formed in
230 water-activated ggbs pastes [14], which is consistent with the higher degree of
231 structural order indicated by XRD and selected area electron diffraction (SAED) in the
232 TEM. These morphologies are essentially unchanged from those observed at 8 years.
233 Similarly, although less common, plates of AFm crystals were again observed intermixed
234 with Op C-A-S-H, as shown in Fig. 6; the identity of the plates was confirmed by EDX
235 analysis. Again as at 8 years, regions of Ip occurred that included distinct laths of the Mg-
236 Al LDH, indicating that the intermixture with C-A-S-H(I) occurred over a range of scales,
237 consistent with results for oPc-ggbs blends [10, 14]; an example is shown in Fig. 7.

238

239 **3.3 Microanalysis of the hydration products**

240 The compositions of the Op and Ip C-A-S-H(I) in the 18-year-old paste are compared in
241 Table 1. TEM-EDX analyses were taken of 33 regions of Op C-A-S-H(I) and 48 of Ip,
242 selected as randomly as possible across the sample. All analyses of Op C-A-S-H(I) were
243 taken from areas established by SAED to be free of intermixture with crystalline phases.

244

245 It is evident that the compositions of the C-A-S-H present in the Op and Ip are essentially
246 identical, except for a greater amount of K in the Op. A scatter plot of Al/Ca against Si/Ca
247 for the individual analyses is shown in Fig. 9(a), which can be compared with the data
248 reported in [12] for 8 years, which are replotted in Fig. 9(b). The comparison reveals the
249 following:

- 250 (i) Whilst the average Si/Ca ratio of the Op C-A-S-H is essentially unchanged
251 between 8 and 18 years, the scatter has reduced, which is reflected in a

252 smaller standard deviation for the Ca/Si reported in Table 1 i.e. at 8 years the
253 Ca/Si = 0.99 ± 0.06 (mean \pm 1 standard deviation; $n = 33$ [12]) but after 18
254 years it is 0.98 ± 0.02 ($n = 33$). This perhaps suggests a tendency with age
255 towards compositional homogenization.

256 (ii) For the 18-year data, the Si/Ca ratio of the Ip C-A-S-H is the same as for the Op
257 C-A-S-H, whereas for the 8-year data it is much lower. This is reflected in the
258 mean values of the Ca/Si ratio reported in Table 1 for 18 years (0.99 ± 0.04 ; n
259 = 48) and in Table 3 of [12] for 8 years (1.18 ± 0.07 ; $n = 34$); the difference in
260 the two values is statistically extremely significant.

261 (iii) Although there are only 7 analyses at 18 years ostensibly of AFm, none of
262 them imply the incorporation of interlayer silicate, which is in contrast to the
263 data for 8 years, which suggest significant interlayer silicate, as has also been
264 observed by TEM-EDX for the AFm in a 5M KOH-activated Pc-20% metakaolin
265 paste [32]. Given the XRD evidence for the reduction in AFm and for the
266 appearance of a hydrogarnet by 18 years, it is plausible that any siliceous
267 AFm (i.e. containing aluminosilicate interlayer anions) had transformed to Si-
268 containing hydrogarnet.

269 Fig. 8 is a scatter plot of Mg/Si against Al/Si atom ratios from EDX analysis of regions of
270 inner product, including analyses from SEM-EDX (filled circles) and TEM-EDX (open
271 circles). The equation that is shown on the figure is from the regression analysis of the
272 SEM-EDX data. A very similar equation was obtained from the TEM-EDX data if
273 restricted to points with Mg/Si < 0.75 (indicated using crosses over the circles); the fact
274 that the TEM-EDX data are offset from the trend line at higher Mg/Si ratios suggest that
275 there may have been a sampling issue with the TEM data, e.g. this could plausibly occur
276 if multiple analyses were inadvertently taken from the Ip regions derived from a small

277 number of slag grains. The results of the regression analysis indicate that $Al/Si = 0.21$ for
278 the Ip C-A-S-H, which is the same as the value determined for the Op C-A-S-H(I), and that
279 $Mg/Al = 2.63$ for the LDH phase, which is in good agreement with the value calculated
280 from the XRD pattern (2.61). The Mg/Al ratios reported in [12] for the 1- and 8-year-old
281 samples were about 2.6 and 2.5 respectively, which means that the Mg/Al ratio of the
282 LDH had probably not changed between 1 and 18 years. The drop at 8 years of about 0.1
283 is unlikely to be significant given the possible sampling issues and the sensitivity of the
284 gradient of the regression line with fairly small datasets.

285 The extra K present in the Op and the fact the Ip consists of intermixture of C-A-S-H with
286 a Mg-Al LDH provides a compositional explanation for the darker greyscale of Ip on BSE
287 images when compared to Op C-A-S-H. BSE imaging provides compositional (average
288 atomic number) contrast with the fraction of electrons that are backscattered, η (called
289 the “backscattering coefficient” = n_{BSE} / n_{PE}), increasing with atomic number [33] (it is
290 commonly calculated using $\eta = -0.0254 + 0.016Z - 1.86 \times 10^{-4}Z^2 + 8.3 \times 10^{-7}Z^3$ [34]). For
291 homogeneous mixtures of elements at the atomic scale $\eta = \sum C_i \eta_i$, where i denotes each
292 constituent, C_i is the mass concentration, and η_i the pure-element backscatter coefficient.
293 Thus on greyscale BSE images regions of high average atomic number appear bright
294 relative to those of lower number and so in the present case the Op C-A-S-H should
295 appear brighter than the Ip because it contains more K and the Ip consists of C-A-S-H
296 that is intimately mixed with the LDH, which contains the lighter elements Mg and Al.
297 The density of particle packing within the hydration product also affects the greyscale
298 (i.e. a more porous product will appear darker) but the evidence from TEM imaging is
299 that the Ip is less porous than the Op.

300

301 **3.4 Nanostructure of C-A-S-H(I)**

302 Fig. 10 shows the single-pulse ^{29}Si NMR spectrum for the 18-year-old sample (centre),
303 the fitted peaks (bottom) and the residual (top). The results of the deconvolution of the
304 spectrum are given in Table 2 and are compared with those for the paste when aged 8
305 years (data taken from Table 4 of [12]). The nature of the aluminosilicate chains and the
306 $Q^n(m\text{Al})$ nomenclature [35] are illustrated in Fig. 3 of [20].

307

308 The Al/Si ratio calculated from the deconvolution of the spectrum is $0.21 \left(\frac{\text{Al}}{\text{Si}} = \right.$
309 $\left. \frac{f}{1-f-v}; [20] \right)$, which is in excellent agreement with the values measured by analytical
310 electron microscopy (Table 1). It is also similar to the value at 8 years (0.19). The
311 additional 10 years of aging resulted in an increase in the MCL from 7.0 to 9.7 i.e. the
312 fraction of vacant tetrahedral sites, v , decreased from about 1 in every 8 sites, to about 1
313 in 11. On the assumption that 'paired' sites in the dreierketten chains cannot be vacant,
314 the occupancy of the 'bridging' sites can be calculated easily using Eqs. 11 and 12 in [20];
315 such calculations show that the increase in MCL was due to the percentage of vacant
316 bridging sites decreasing from 37% to 28%; the ratio of bridging sites that were
317 occupied by Al to those occupied by Si was about 2:1 at both ages (see the site
318 occupancy factors given in Table 2).

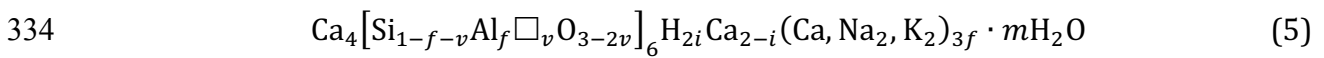
319
320

321 Fig. 11 (top) shows the ^{27}Al NMR spectrum of the 18-year-old specimen. It is very similar
322 to the one obtained for the paste at the age of 8 years (bottom), with two large peaks:
323 one for Al that is tetrahedrally co-ordinated (labelled "Tet."), due predominantly to Al
324 that is substituted for Si in the C-A-S-H(I), and the other for Al that is octahedrally co-
325 ordinated (labelled "Oct.") that is due to the Mg-Al LDH. The peaks are rather broader on
326 the spectrum for the older paste, which is to be expected because it was collected using a

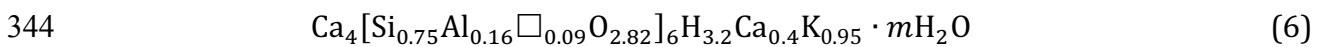
327 lower magnetic field [36]. The up-field shoulder on the Al^[6] peak at 8 years that was
 328 attributed to the AFm phase is not evident for the 18-year-old paste, and whilst its
 329 presence might have been obscured by the reduced resolution, a smaller amount of AFm
 330 is consistent with the XRD evidence (§3.1).

331

332 Richardson [20] showed that single-chain tobermorite or C-A-S-H(I) can be represented
 333 by the generalized structural-chemical formula:



335 Where the aluminosilicate part of the structure is within the square brackets (the □
 336 represents a vacant tetrahedral site; v is the fraction of tetrahedral sites that are vacant;
 337 f is the fraction that are occupied by Al), there are 4 main-layer Ca atoms for every 6
 338 tetrahedral sites, and the value of i reflects the extent to which the net charge is
 339 balanced by protons or Ca²⁺ ions. The contents of the round brackets are additional
 340 interlayer ions that are needed to charge-balance the Al³⁺ substitution for Si⁴⁺, in the
 341 present case, K⁺ ions. Substitution of the values in Table 2 for v and f and calculation of i
 342 from the Ca/Si ratio gives the following approximate formula for the C-A-S-H(I) in the
 343 18-year-old paste (Ca/Si = 0.98; Al/Si = 0.21; (Ca+K)/Si = 1.19; MCL = 10):



345

346 **4. Conclusions**

347 The main hydration products present in an 18-year-old 5M KOH-activated ggbs paste
 348 were the same as reported previously for the paste at 8 years: semi-crystalline C-A-S-
 349 H(I) that was present in both inner and outer product regions; and a Mg-Al layered
 350 double hydroxide that was present in the inner product region intermixed on a range of

351 scales with the C-A-S-H(I). The morphologies of these two phases had not changed with
352 time. In addition, a reduced quantity of an AFm phase was observed, although it no
353 longer appeared to contain silicate. It is possible that the siliceous AFm present at 8
354 years had transformed to hydrogarnet by 18 years. The Op and Ip C-A-S-H(I) had the
355 same chemical composition at 18 years. The Ca/Si ratio of the Op C-A-S-H(I) was
356 unchanged from 8 years but the value for the Ip was significantly lower. Reduced scatter
357 in the data is suggestive of a tendency towards compositional homogeneity with age.
358 The mean length of the aluminosilicate chains in the C-A-S-H(I) increased from 7.0 at 8
359 years to 9.7 at 18 years of age, which corresponded to a reduction in the percentage of
360 vacant bridging sites in the dreierketten chains from 37% at 8 years to 28% at 18 years.
361 The ratio of the bridging sites occupied by Al to those occupied by Si was about 2:1 at
362 both ages. The layer spacings of both the C-A-S-H(I) and Mg-Al LDH phases did not
363 change significantly with age (about 12.7 Å and 7.7 Å respectively). The Mg/Al ratio of
364 the LDH was about 2.6 and had not changed significantly between 1 and 18 years.

365

366 **Acknowledgments**

367 Thanks are due to the UK's Nuclear Decommissioning Authority for funding the work,
368 including the provision of a fully funded studentship for SL at the University of Leeds.

369

370 **References**

371

- 372 [1] Department of Energy and Climate Change, Implementing Geological Disposal - A
373 framework for the long term management of higher activity waste, URN
374 14D/235, July 2014.

- 375 [2] F.P. Glasser, Progress in the immobilization of radioactive wastes in cement, *Cem.*
376 *Concr. Res.*, 22 (1992) 201-216.
- 377 [3] M. Atkins, F. Glasser, Application of Portland cement-based materials to
378 radioactive waste immobilization, *Waste Management*, 12 (1992) 105-131.
- 379 [4] F. Glasser, M. Atkins, Cements in radioactive waste disposal, *MRS Bulletin*, 19
380 (1994) 33-38.
- 381 [5] Serco, Cement materials for use as backfill, sealing and structural materials in
382 geological disposal concepts, SERCO/005125/001 Issue 3, 2012.
- 383 [6] P. Faucon, F. Adenot, J.F. Jacquinot, J.C. Petit, R. Cabrillac, M. Jorda, Long-term
384 behaviour of cement pastes used for nuclear waste disposal: review of physico-
385 chemical mechanisms of water degradation, *Cem. Concr. Res.*, 28 (1998) 847-857.
- 386 [7] Nuclear Decommissioning Authority, Near-field evolution status report, NDA report
387 NDA/RWMD/033, 2010.
- 388 [8] C.R. Wilding, G. McHugh, The hydration of blast-furnace slag cements. UK Atomic
389 Energy Authority Report AERE R 12297, PETF(86)P27 (1986).
- 390 [9] I.G. Richardson, C.R. Wilding, M.J. Dickson, The hydration of blastfurnace slag
391 cements, *Adv. Cem. Res.*, 2 (1989) 147-157.
- 392 [10] I.G. Richardson, G.W. Groves, The microstructure and microanalysis of hardened
393 cement pastes involving ground granulated blast-furnace slag, *J. Mater. Sci.*, 27
394 (1992) 6204-6212.
- 395 [11] I.G. Richardson, G.W. Groves, The microstructure and microanalysis of hardened
396 ordinary Portland cement pastes, *J. Mater. Sci.*, 28 (1993) 265-277.
- 397 [12] I.G. Richardson, A.R. Brough, G.W. Groves, C.M. Dobson, The characterization of
398 hardened alkali-activated blast-furnace slag pastes and the nature of the calcium
399 silicate hydrate (C-S-H) phase *Cem. Concr. Res.*, 24 (1994) 813-829.

- 400 [13] R. Taylor, I.G. Richardson, R.M.D. Brydson, Composition and microstructure of 20-
401 year old neat Portland cement and 10% Portland cement-90% ggbs pastes, *Adv.*
402 *Appl. Ceram.* 106 (2007) 294–301.
- 403 [14] R. Taylor, I.G. Richardson, R.M.D. Brydson, Composition and microstructure of 20-
404 year-old ordinary Portland cement-ground granulated blast-furnace slag blends
405 containing 0 to 100% slag. *Cem. Concr. Res.* 40 (2010) 971-983.
- 406 [15] K.L. Scrivener, V.M. John, E.M. Gartner. Eco-efficient cements: Potential,
407 economically viable solutions for a low-CO₂, cement-based materials industry.
408 United Nations Environment Programme, Paris, 2016.
- 409 [16] C. Shi, P.V. Krivenko, D. Roy. Alkali-activated cements and concretes. Taylor &
410 Francis, 2006.
- 411 [17] Heller, L., Taylor, H.F.W. (1956) Crystallographic data for the calcium silicates,
412 79pp., London: HMSO.
- 413 [18] Koritnig, S., Süsse, P. (1975) Meixnerite, Mg₆Al₂(OH)₁₈·4H₂O, ein neues
414 Magnesium-Aluminium-Hydroxid Mineral. *Tschermaks Mineralogische und*
415 *Petrographische Mitteilungen* 22, 79-87.
- 416 [19] J.A. Chudek, G. Hunter, M.R. Jones, S.N. Scrimgeour, P.C. Hewlett, A.B. Kudryavtsev,
417 Aluminium-27 solid state NMR spectroscopic studies of chloride binding in
418 Portland cement and blends, *J. Mater. Sci.* 35 (2000) 4275–4288.
- 419 [20] I.G. Richardson. Model structures for C-A-S-H(I), *Acta Cryst.* B70 (2014) 903-923.
- 420 [21] G. Mascolo, O. Marino, A new synthesis and characterization of magnesium-
421 aluminium hydroxides. *Miner. Mag.* 43 (1980) 619-621.
- 422 [22] Roberts, M.H. (1969) Calcium aluminate hydrates and related basic salt solid
423 solutions. *5th Int. Symp. Chem. Cem., Vol. 2*, 104-117.
- 424 [23] Taylor, H.F.W. (1997) *Cement Chemistry*, 2nd Edition, Thomas Telford, London.

- 425 [24] L.S. Wells, W.F. Clarke, H.F. McMurdie, Study of the system $\text{CaO}-\text{Al}_2\text{O}_3-\text{H}_2\text{O}$ at
426 temperatures of 21° and 90 °C, J. Res. Nat. Bureau Standards (1943) 367–407.
- 427 [25] T. Matschei, B. Lothenbach, F.P. Glasser. The AFm phase in Portland cement. Cem.
428 Concr. Res. 37 (2007) 118-130.
- 429 [26] F. Bonk, J. Schneider, M.A. Cincotto, H. Panepucci. Characterization by
430 multinuclear high-resolution NMR of hydration products in activated blast-
431 furnace slag pastes. J. Am. Ceram. Soc. 86 (2003) 1712-1719.
- 432 [27] V.A.Drits, A.S. Bookin. Crystal structure and X-ray identification of layered double
433 hydroxides. In V. Rives, ed. Layered Double Hydroxides: Present and Future. Nova
434 Science Publishers, Inc. Ch. 2, 41–100 (2001).
- 435 [28] I.G.Richardson, The importance of proper crystal-chemical and geometrical
436 reasoning demonstrated using layered single and double hydroxides. Acta Cryst
437 B69 (2013) 150–162.
- 438 [29] R.D. Shannon. Revised effective ionic radii and systematic studies of interatomic
439 distances in halides and chalcogenides. Acta Cryst. A, 32 (1976) 751-767.
- 440 [30] J.H. Taplin, A method for following the hydration reaction in Portland cement
441 paste, Australian Journal of Applied Science, 10 (1959) 329-345.
- 442 [31] A.R. Brough, A. Atkinson. Sodium silicate-based, alkali-activated slag mortars,
443 Part I. Strength, hydration and microstructure. Cem. Concr. Res. 32 (2002) 865-
444 879.
- 445 [32] I.G. Richardson, J. Skibsted, L. Black, R.J. Kirkpatrick. Characterisation of cement
446 hydrate phases by TEM, NMR and Raman spectroscopy, Adv. Cem. Res. 22 (2010)
447 233-248.

- 448 [33] K.F.J. Heinrich, Proceedings of the 4th International Conference on X-ray optics
449 and microanalysis, Ed. R. Castaing, P. Deschamps, J. Philibert, Hermann, Paris
450 (1966) 159.
- 451 [34] W. Reuter, The ionization function and its application to the electron probe
452 analysis of thin films, Proceedings of the 6th International conference on X-ray
453 optics and microanalysis, Ed. G. Shinoda, K. Kohra, T. Ichinokawa, University of
454 Tokyo Press, (1972) 121.
- 455 [35] G.Engelhardt and D.Michel, High resolution solid state NMR of silicates and
456 zeolites, Wiley (1987).
- 457 [36] M.D. Andersen, H.J. Jakobsen, J. Skibsted, Incorporation of aluminum in the
458 calcium silicate hydrate (C-S-H) of hydrated Portland cements: A high-field ²⁷Al
459 and ²⁹Si MAS NMR investigation. Inorganic Chemistry 42 (2003) 2280-2287.

460

461 **Table and Figure Captions**

462

463 **Table 1.** The Ca/Si, Al/Si and (Ca+K)/Si atom ratios of Op and Ip C-A-S-H. The values
464 were determined by TEM-EDX except for the Al/Si ratio of the Ip C-A-S-H and the Mg/Al
465 ratio of the Mg-Al LDH, which were determined by regression analysis of SEM-EDX data,
466 (as illustrated in Fig. 8), and the average Al/Si ratio for all of the C-A-S-H that was
467 calculated from the results of the deconvolution of the ²⁹Si NMR spectrum (as outlined in
468 §3.4).

469

470 **Table 2.** Results of deconvolution (by least-squares-fitting) of the single-pulse ²⁹Si NMR
471 spectra for the pastes aged 8 and 18-years, the former taken from Table 4 of [12].
472 Fractions of silicon present in different tetrahedral environments, Qⁿ(mAl) [35]; the

473 mean aluminosilicate chain length (MCL, calculated using Eq. 1 in [12]); the fractions of
474 tetrahedral sites that are vacant (v) or occupied by Al (f) were calculated using Eqs. 4
475 and 8 respectively from [20] and the bridging site occupancy factors using Eqs. 11 (for
476 Si) and 12 (for Al). *calculated excluding a small fraction (0.015) for Q^3 .

477

478 **Figure 1.** Powder XRD data. The full pattern ($5-70^\circ 2\theta$) is of the 18-year-old 5M KOH-
479 activated ggbs paste, which was acquired using the equipment and parameters given in
480 §2.2. The positions of the major peaks for two main phases present in the paste are
481 indicated with arrows, labelled “C” for the C-A-S-H(I) phase [17], and “M” for the Mg-Al
482 layered double hydroxide (LDH) [18]; the layer-spacings for the two phases are
483 indicated, as is the value of d_{110} for the Mg-Al LDH phase. The three inset patterns
484 plotted between $4-14^\circ 2\theta$ are for 5M KOH-activated pastes using the same ggbs
485 hydrated for 7 days (labelled “7d”), 4 months (“4m”), and 8 years (“8y”); again, the layer-
486 spacings for the C-A-S-H(I) and Mg-Al LDH phases are indicated. The first two patterns
487 were extracted from Fig. 7 of [8] and the third was extracted from Fig. 1 of [12]. The
488 inset pattern plotted between $15-46^\circ 2\theta$ is of the anhydrous ggbs (labelled “S”), which
489 was extracted from Fig. 3 of [8]. The glassy nature of the ggbs is evident from the halo on
490 the pattern; the largest peak of the only crystalline phase present in the ggbs, melilite, is
491 labelled “ml”.

492

493 **Figure 2.** Cumulative particle size distribution for the ggbs determined by laser
494 granulometry. Points correspond to the mass % below the indicated particle size i.e.
495 4.4% of the particles are finer than $1\ \mu\text{m}$. Values for the median particle size and the
496 Rosin-Rammler constants are indicated (n is a measure of the breadth of distribution

497 (higher n = narrower distribution); x_0 is a measure of the average size (36.8% of
498 particles are $> x_0$)).

499

500 **Figure 3.** DTA, TG and evolved gas analysis curves for the sample.

501

502 **Figure 4.** Typical backscattered electron image showing unreacted slag (S), inner
503 product (Ip) and outer product (Op). The cracks are an artefact of specimen preparation.

504

505 **Figure 5.** TEM micrograph of a region in the 18-year-old paste that illustrates Op C-A-S-
506 H with foil-like morphology sandwiched between two regions of Ip.

507

508 **Figure 6.** TEM micrograph of a region in the 18-year-old paste that illustrates plates of
509 AFm crystals embedded between Ip and Op C-A-S-H.

510

511 **Figure 7.** TEM micrograph of a region in the 18-year-old paste that illustrates distinct
512 laths of Mg-Al LDH intermixed with Ip C-A-S-H.

513

514 **Figure 8.** Mg/Si against Al/Si atom ratios from EDX analysis of regions of inner product
515 in the SEM (filled circles) and TEM (open circles). The equation is from the regression
516 analysis of the SEM-EDX data.

517

518 **Figure 9.** Al/Ca against Si/Ca atom ratio plot of TEM microanalyses of Op C-A-S-H (+),
 519 inner product (circles) and AFm crystals (unfilled triangles) for (a) the 18-year-old
 520 sample, and (b) the 8-year-old sample (replotted from [12]). A filled triangle indicates
 521 the ideal composition for silicate-free AFm phases and the ideal composition of
 522 strätlingite (C₂ASH₈) is indicated by a square symbol. The dotted tie-line is drawn
 523 between AFm and Op C-A-S-H (at Si/Ca = 1 and Al/Ca = 0.2) and the dashed tie line is
 524 drawn between AFm and strätlingite.

525

526 **Figure 10.** Single pulse ²⁹Si MAS NMR spectrum for the 18-year-old KOH-activated paste
 527 (middle), the fitted peaks (bottom), and the residual (top). The chemical shifts of the
 528 fitted peaks (in ppm) in the order Q^{slag} (i.e. unreacted slag), Q¹, Q²(1Al), Q²(0Al) are: –
 529 75.8, –79.8, –82.4, and –85.3 ppm. There is the possibility of a small amount of Q³ (in this
 530 fit, 1.5%, chemical shift –89.4 ppm).

531

532 **Figure 11.** Single-pulse ²⁷Al MAS NMR spectrum for the 5M KOH-activated ggbs paste
 533 aged 8 years (bottom, reproduced from [12]) and 18 years (top).

534

535

	<i>n</i>	Ca/Si		Al/Si		NMR	(Ca+K)/Si		Mg/Al
		Mean	S.D.	Mean	S.D.		Mean	S.D.	
Op	33	0.98	0.02	0.21	0.02		1.25	0.05	
Ip	48	0.99	0.04	0.21*	/		1.17	0.06	2.63*
All	81	0.99	0.03	/	/	0.21	1.21	0.06	

536

537 **Table 1.**

538

539

Age	Q^{slag}	Q^1	$Q^2(1Al)$	$Q^2(0Al)$	MCL	f	v	SOF_{BT}^{Si}	SOF_{BT}^{Al}	SOF_{BT}^V
8y	0.225	0.262	0.299	0.214	7.1	0.142	0.124	0.20	0.43	0.37
18y	0.209	0.194	0.329	0.253	9.7*	0.159	0.094	0.24	0.48	0.28

540

541 **Table 2.**

542

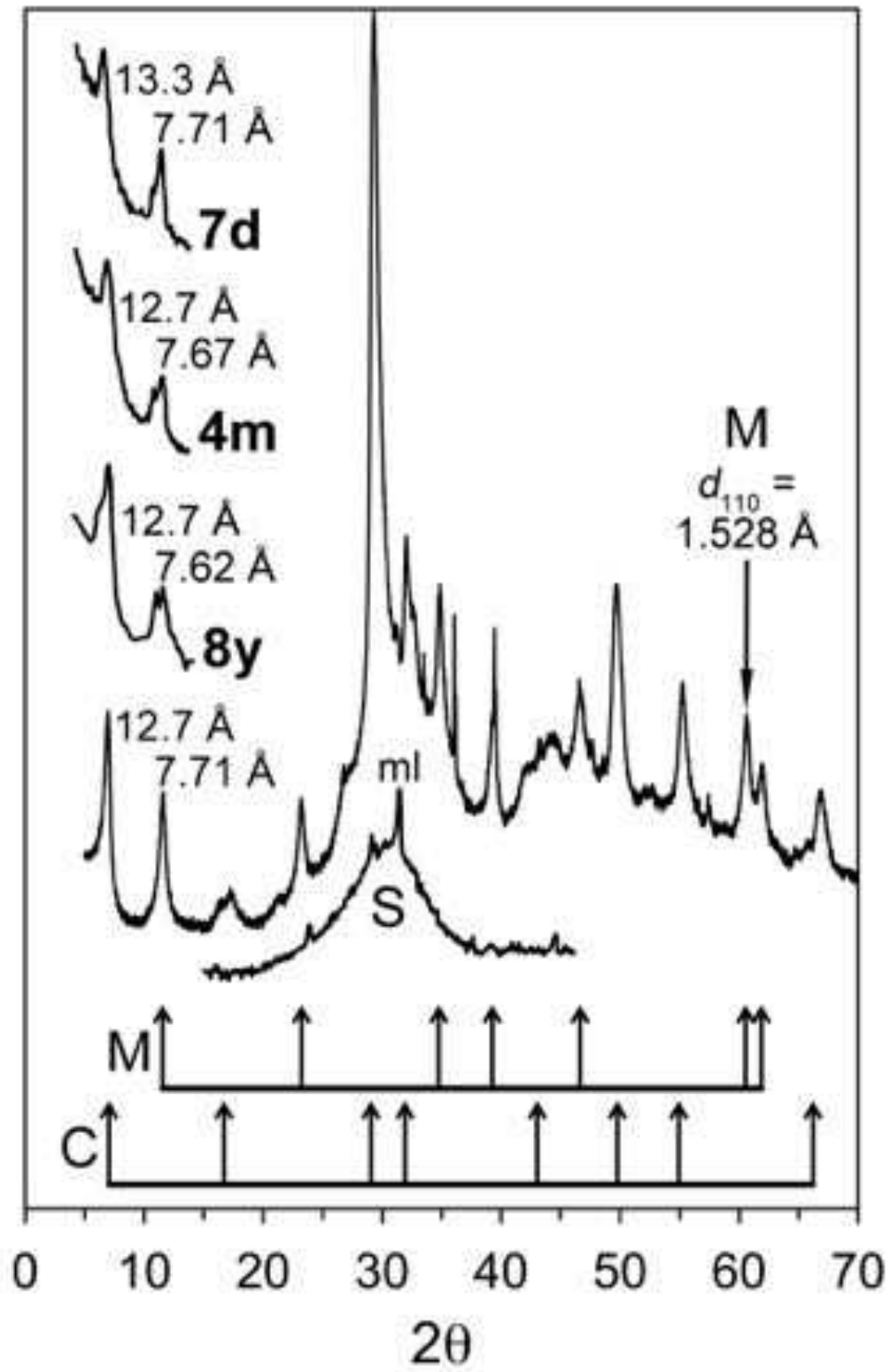


Fig. 1

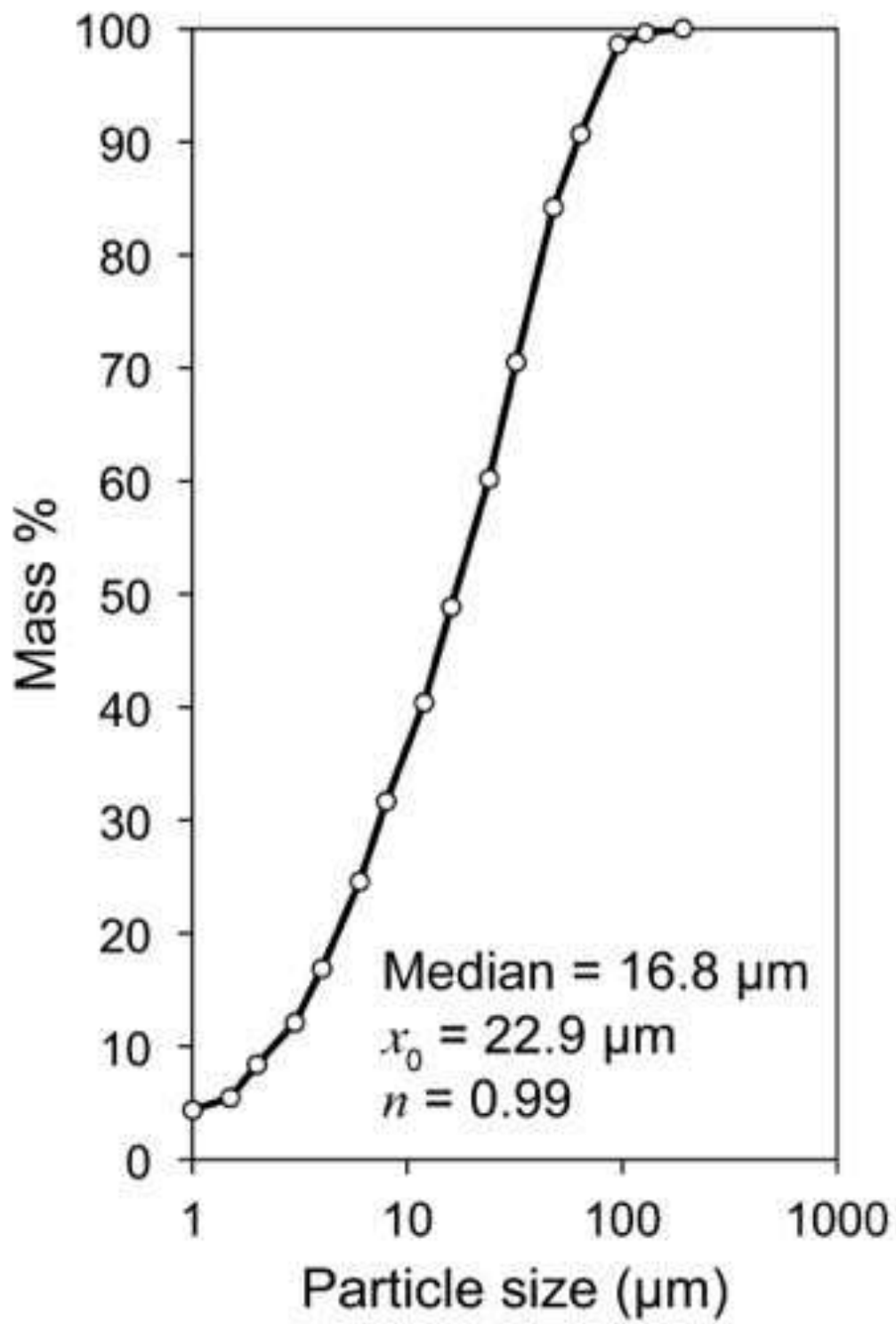


Fig. 2

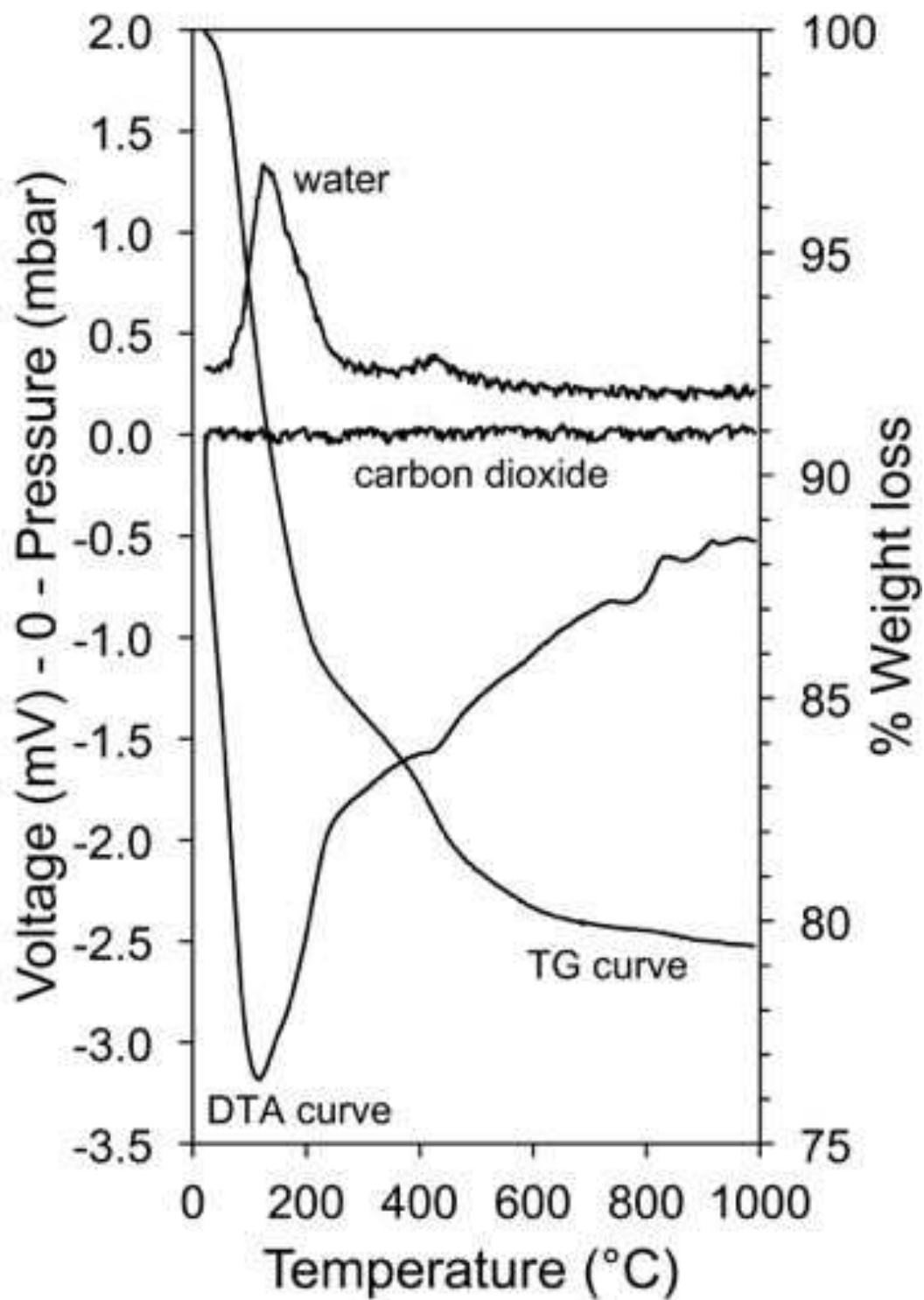


Fig. 3

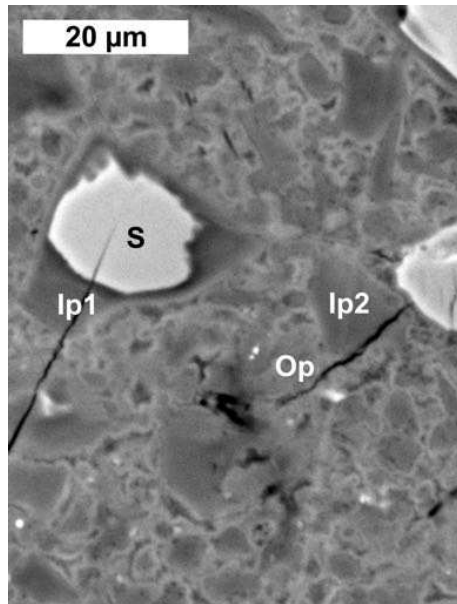


Fig. 4

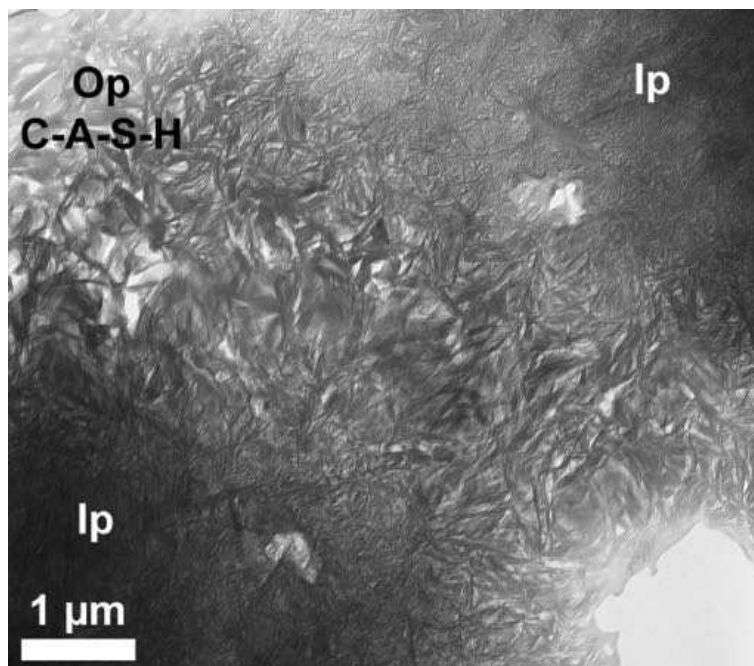


Fig. 5

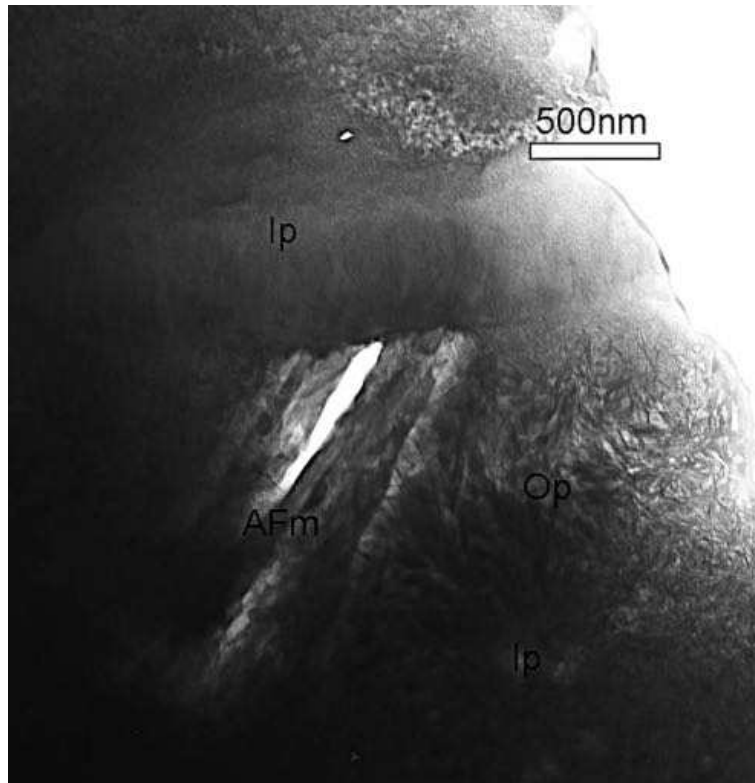


Fig. 6

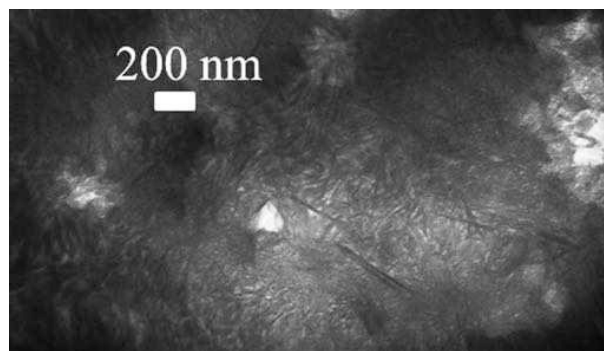


Fig. 7

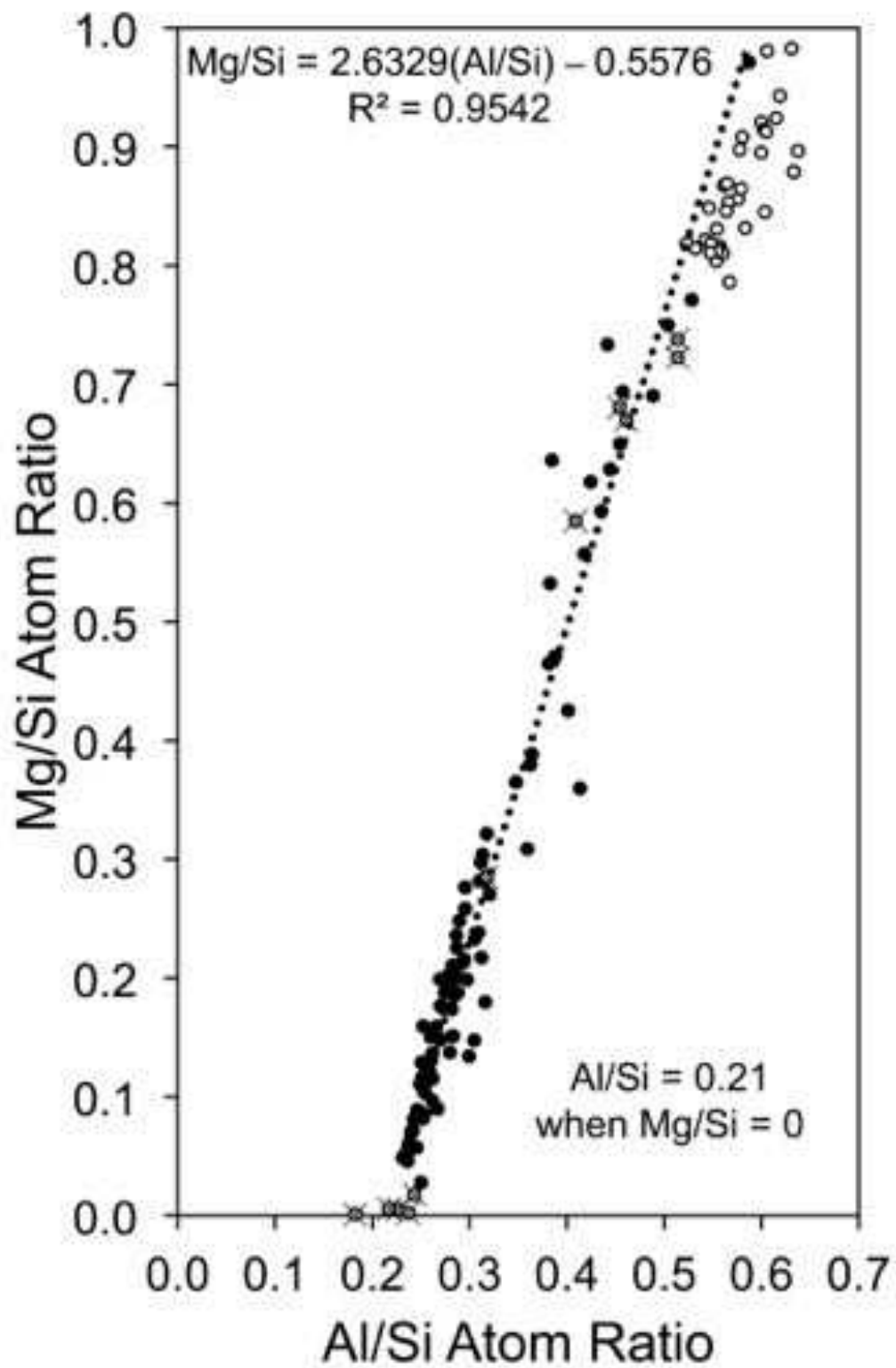


Fig. 8

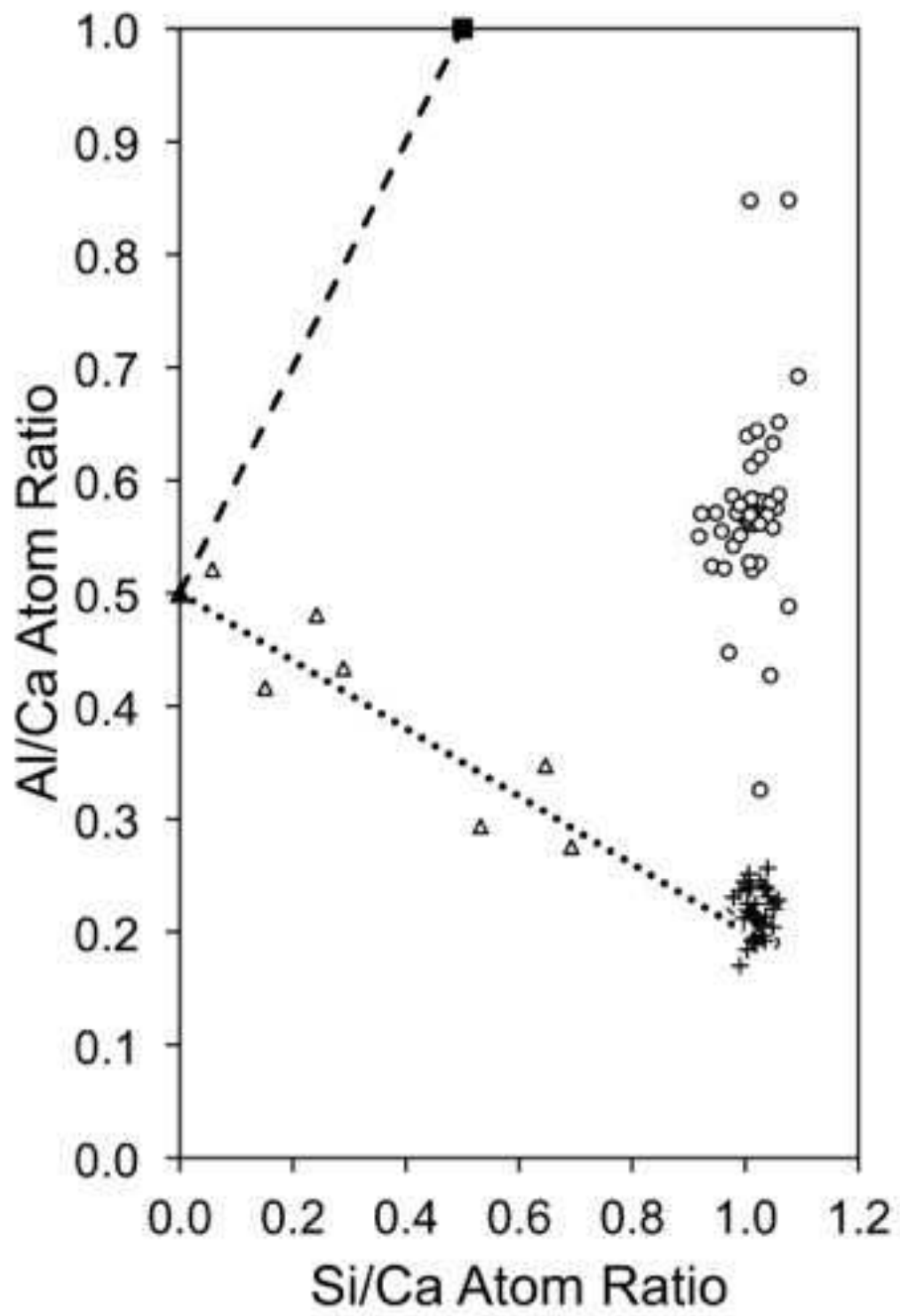


Fig. 9a

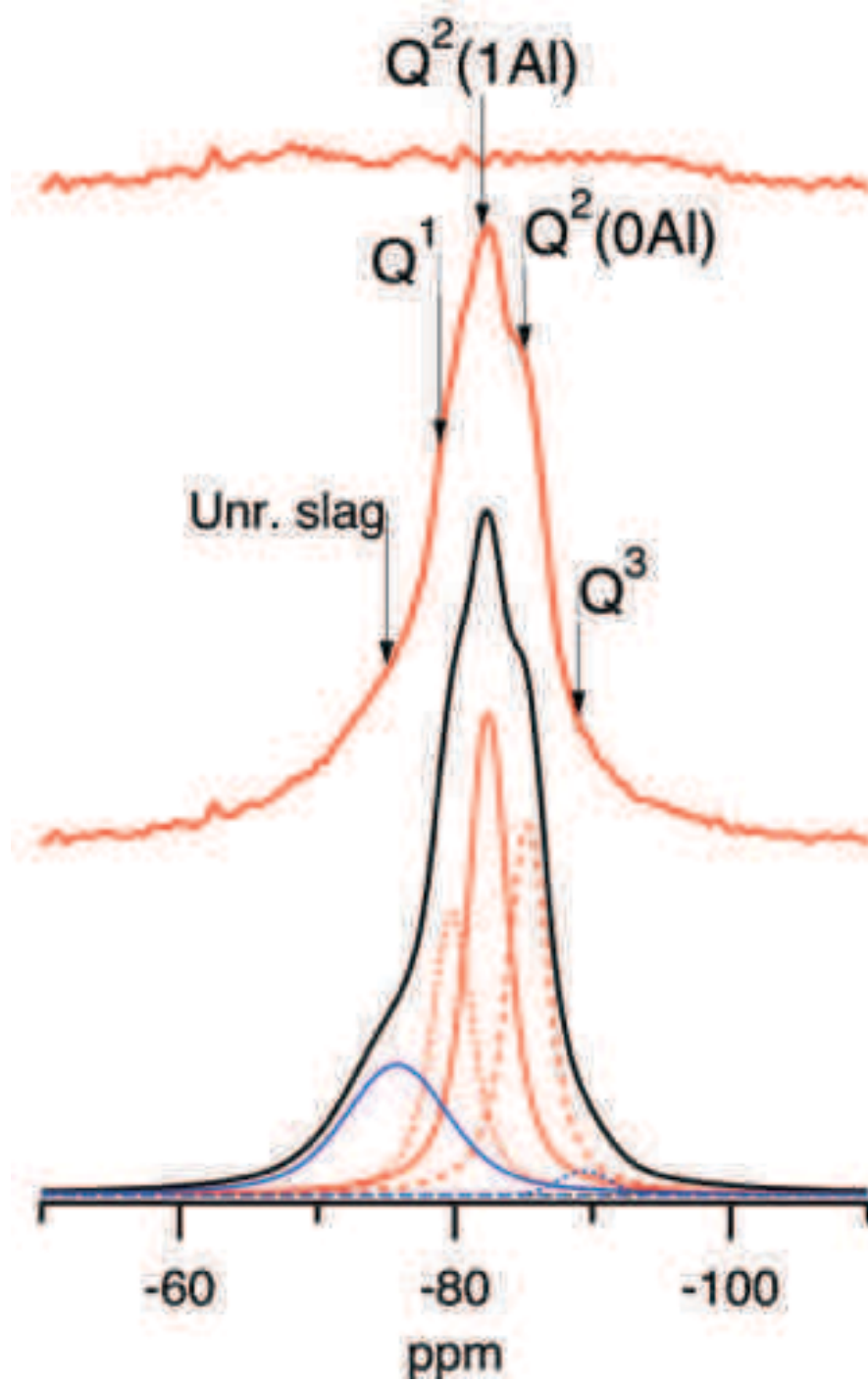


Fig. 10

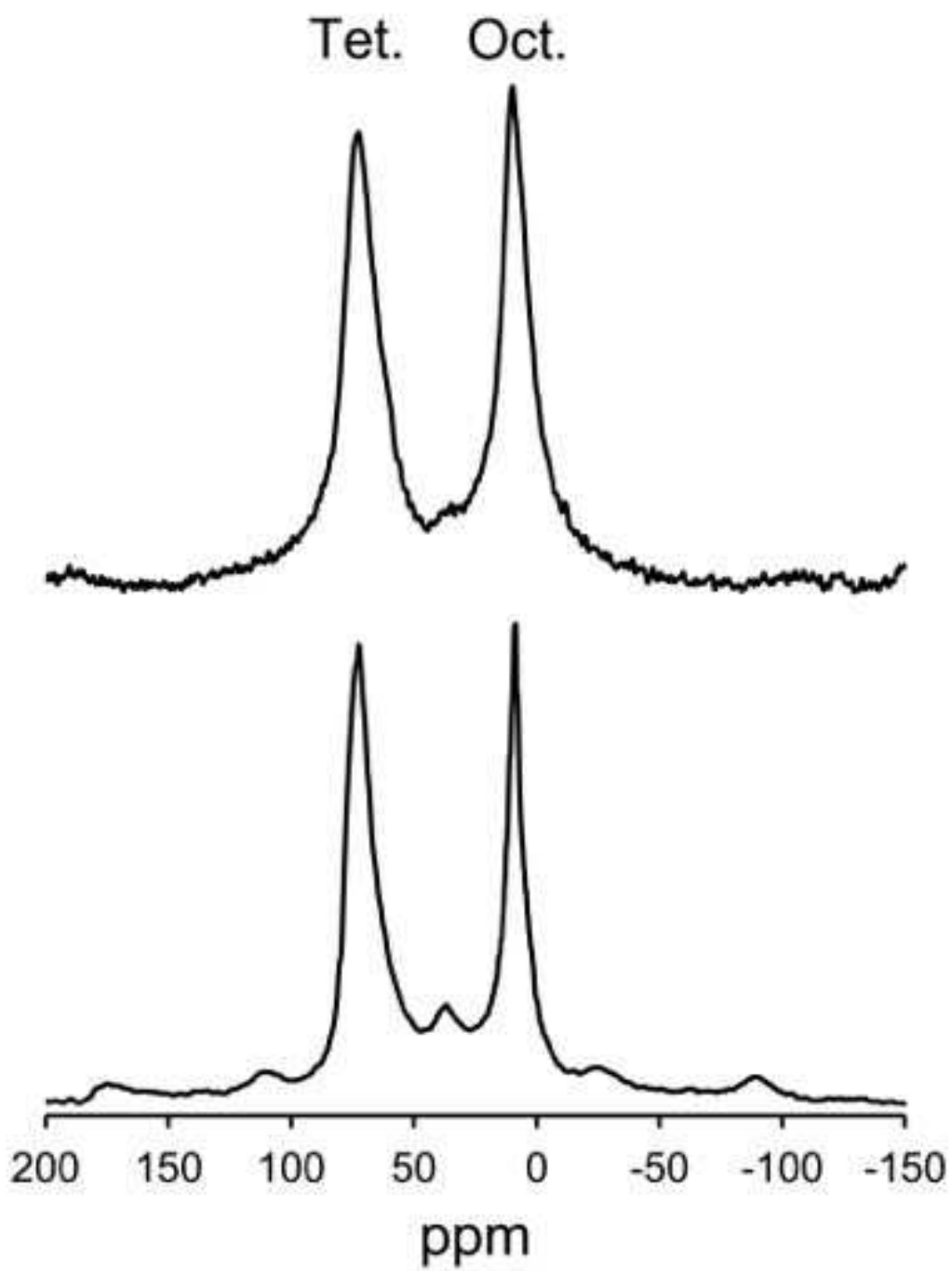


Fig. 11

543